Inorganica Chimica Acta 574 (2025) 122395

Contents lists available at ScienceDirect

Inorganica Chimica Acta

journal homepage: www.elsevier.com/locate/ica

Enhancing formate yield through electrochemical CO_2 reduction using BiOCl and g-C_3N_4 hybrid catalyst

Smritirekha Talukdar [a], Manuela Bevilacqua [b], Enqi Bu [c], Lapo Gabellini [d], Lapo Querci [d], Juan Josè Delgado [c], Matteo Mannini [d], Paolo Fornasiero [a], Tiziano Montini [a,*]

[a] Department of Chemical and Pharmaceutical Sciences, Centre for Energy, Environment and Transport Giacomo Ciamician, Consortium INSTM, Trieste Research Unit and ICCOM-CNR Trieste Research Unit, University of Trieste, Via L. Giorgieri 1, 34127 Trieste, Italy
[b] Institute of Chemistry of Organometallic Compounds (ICCOM), National Research Council (CNR), Via Madonna del Piano 10, 50019 Sesto Fiorentino (FI), Italy
[c] Departamento de Ciencia de los Materiales, Ingeniería Metalúrgica y Química Inorgánica, Instituto Universitario de Investigación en Microscopía Electrónica y Materiales (IMEYMAT), Universidad de Cádiz, Campus Río San Pedro, Puerto Real (Cádiz), 11510, Spain
[d] Department of Chemistry "U. Schiff" (DICUS), University of Florence and and Consortium INSTM, Firenze Research Unit, via della Lastruccia 3-13 50019, Sesto Fiorentino (FI), Italy

ARTICLE INFO

Dedicated to Dr. Francesco Vizza

Keywords:
$BiOCl/g\text{-}C_3N_4$
Electrocatalysis
CO_2 reduction
Formate
Selectivity

ABSTRACT

Electrochemical carbon dioxide (CO_2) reduction with bismuth-based catalysts has been widely investigated in the recent few years. This is due to bismuth's ability to perform selective electrochemical CO_2 reduction reaction (eCO_2RR) to an important C_1 product, the formate ($HCOO^-$). However, boosting the performance of such catalysts is a continuous investigation. In this work, enhancing the active sites for eCO_2RR is investigated by forming nanocomposites with graphitic carbon nitride (g-C_3N_4). BiOCl is synthesized by a simple wet-chemical approach in the presence of glycine as size-controlling agent and formed into nanocomposites, which were characterized by Scanning Electron Microscopy (SEM), X-ray diffraction (XRD), Raman spectroscopy, X-ray photoelectron spectroscopy (XPS), Infrared (IR) Spectroscopy and N_2 physisorption. Linear Sweep Voltammetry (LSV) in argon and CO_2-saturated atmosphere showed higher current values in the case of CO_2. Chronoamperometries (CA) were recorded at −1.06 V vs Reversible Hydrogen Electrode (RHE) for 5400 s obtaining Faradic Efficiencies (FE) varying in the range of 70–77 % depending on the nanocomposites' composition. In fact, 52.1 wt% $BiOCl/g\text{-}C_3N_4$ formed the highest yields for formate (with also the highest rate of formation of formate) together with a minimal production of H_2 and CO. The effect of nano-structuration induced by glycine, used as a size-controlling agent, to form nanoplates was crucial: microplates of BiOCl produced without glycine showed an FE of 4 %, reaching 85 % in the case of the nanoplates. Post-electrocatalysis characterization revealed the possible role of $Bi_2O_2CO_3$ as the active phase for eCO_2RR.

1. Introduction

There has been a lot of research ongoing to find an efficient, selective, durable, and low-cost catalyst for electrochemical CO_2 reduction reaction (eCO_2RR) to other carbon-based products [1–3]. In recent years, the value of formic acid has increased due to the world's inclination toward the hydrogen economy [4–6]. It can be attributed to the fact that formic acid is a viable and suitable H_2 carrier. This is due to its high volumetric capacity of 53 g H_2/L given by its high density of 1.22 g. cm^{-3} in addition to low toxicity and flammability [7,8]. Moreover, the distribution cost of H_2 is reported to have been cut by 12 % by eCO_2RR obtaining formic acid in comparison with the thermocatalytic process [8]. This benefits us in reducing excessive CO_2 emissions as well as obtaining a Liquid Hydrogen Carrier (LHC) that brings us closer to a carbon–neutral economy.

Product selectivity is an essential parameter necessary to understand the performance of the catalyst. It was reported in 2020 by Yang et al. that the *p*-block metal-based electrocatalysts were responsible for selectively reducing CO_2 to $HCOO^-$. The characteristic oxophilicity of p-block metals leads to the formation of *OCHO over *COOH, which has been shown to be the key intermediate in the formation of formate or formic acid [9]. Amongst recent literature, eCO_2RR, leading to formate using gas-diffusion electrodes, using these *p*-block metals was reported. It was shown in the study that indium, tin, and bismuth had FE values of

* Corresponding author.
E-mail address: tmontini@units.it (T. Montini).

https://doi.org/10.1016/j.ica.2024.122395
Received 29 June 2024; Received in revised form 19 September 2024; Accepted 25 September 2024
Available online 26 September 2024

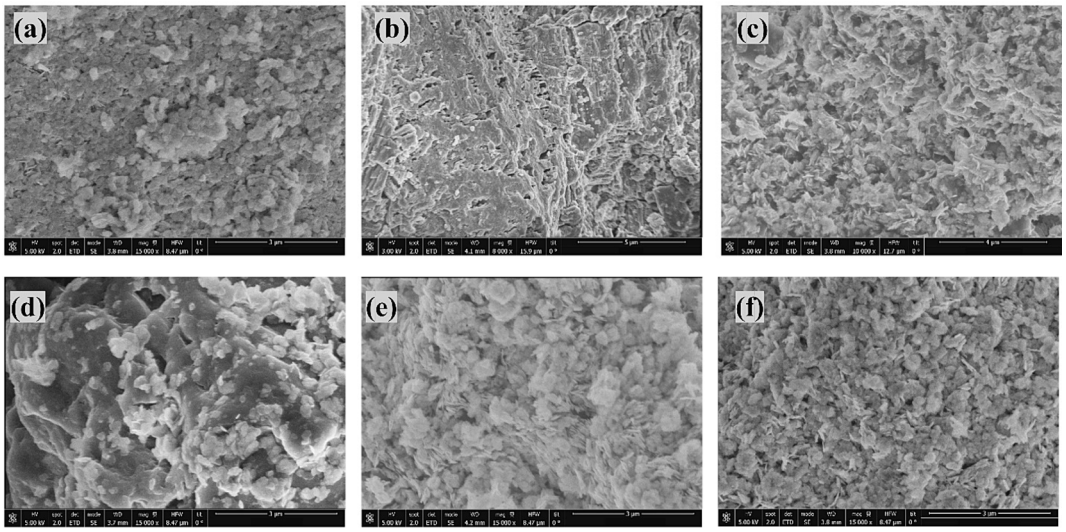

Fig. 1. Representative SEM images of (a) BiOCl (b) g-C_3N_4 (c) 52.1 % BCN (d) 12 % BCN (e) 71.2 % BCN (f) 80.1 % BCN.

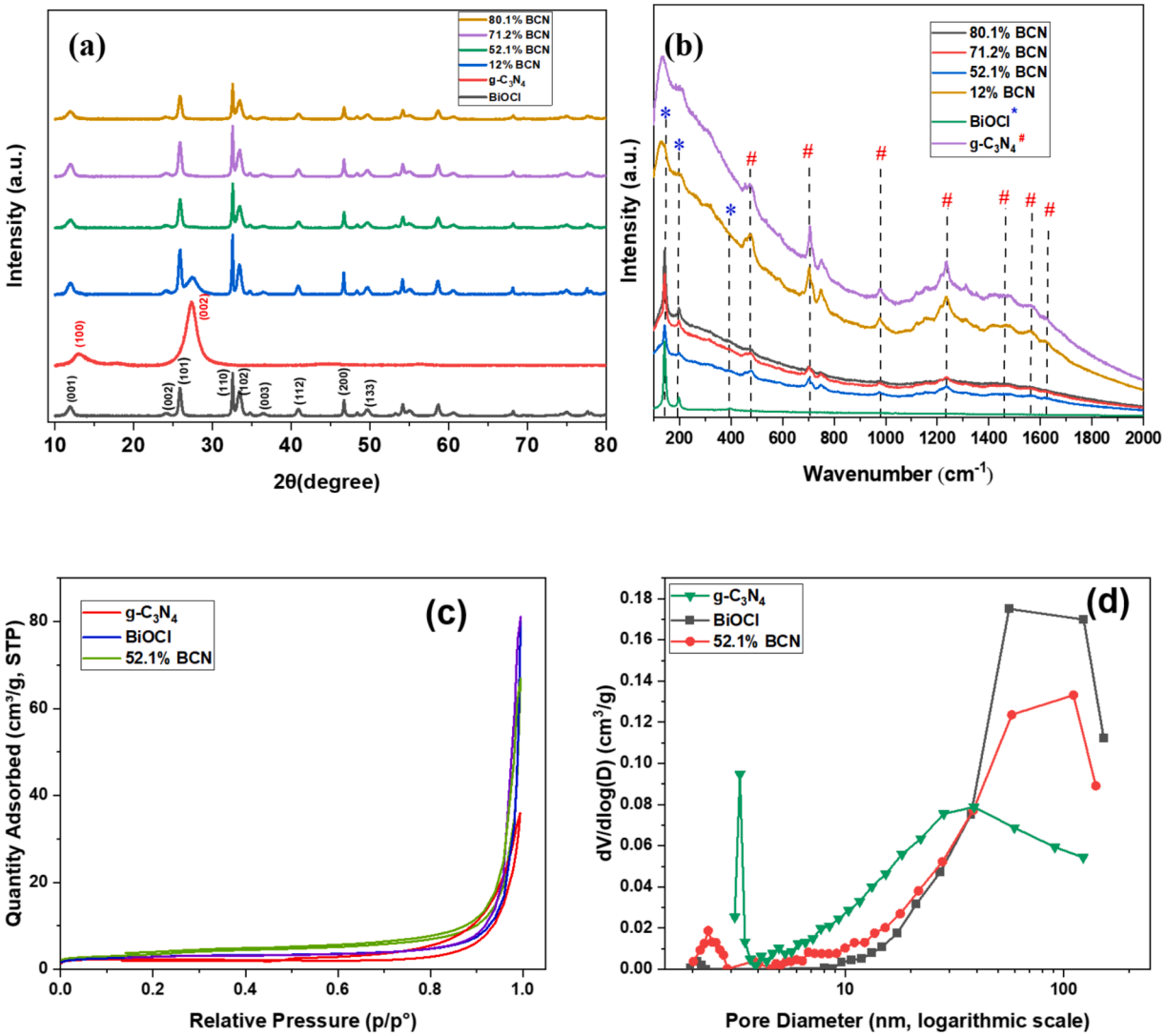

Fig. 2. Characterization of the synthesized materials: (a) XRD patterns, (b) Raman spectra of all the materials; (c) N_2 sorption isotherm, and (d) BJH pore-size distribution of g-C_3N_4, BiOCl and 52.1 % BCN.

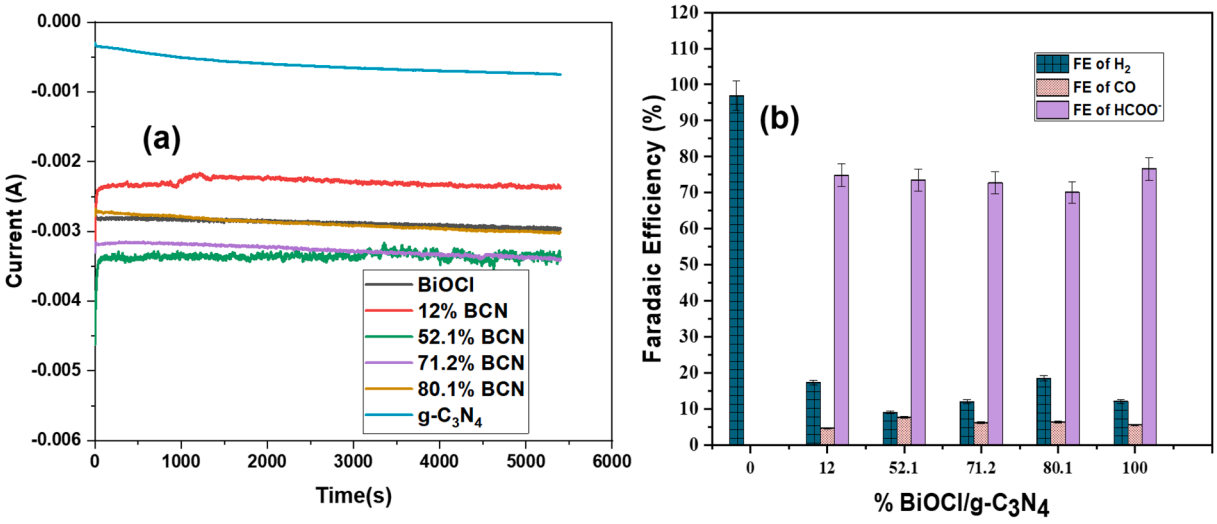

Fig. 3. Electrochemical CO_2 reduction tests at −1.06 V vs RHE for 5400 s using gas-tight cell (a) CA analyses. (b) FEs of different products H_2, CO, and $HCOO^-$ of all the catalysts with CA analysis of 5400 s.

> 80 % whereas cadmium and lead catalysts equated for < 80 % [10]. Bismuth-based materials have high selectivity for formate; synthesis strategies enhancing their activity and selectivity [11–15], with control of the morphology to expose most of the active facets [16] have been described. Among the bismuth oxyhalides i.e. BiOX (X = Cl, Br, and I), BiOCl is seen to have much interest for eCO_2RR. It was studied in 2021 by Hsieh et al. that Pd-doped BiOCl nanosheets, prepared by a wet-chemical approach, had an FE of 30 % for $HCOO^-$ from eCO_2RR [17]. BiOCl was transformed into its subcarbonate chloride form by electro-reduction which accounted for 97.9 % of FE for formate while pure $Bi_2O_2CO_3$ accounted for 81.3 % FE for formate [18]. In another study, *N*-doped carbon with BiOCl dispersed resulted in 84.3 % of FE for formate [19]. g-C_3N_4 is a type of carbon-nitride that has a 2D lamellar polymeric structure comprising triazine and heptazine rings. It is a widely used semiconductor in photocatalysis [20]. However, recent studies can be seen where its electrocatalytic role has also been explored [20–22]. Nazir et al. in 2020 reported the use of carbon-nitride based nano-composites for the production of formic acid by eCO_2RR. It was found that g-C_3N_4/CuAg/Cu_2O had higher selectivity for formic acid when compared to g-C_3N_4/Cu/Cu_2O [23]. Cu-doped carbon-nitride was reported for electrocatalytic Oxygen Reduction Reaction (ORR), showing good electrocatalytic response as a cathode in an alkaline environment. It showed an onset potential of 0.92 V vs RHE with long-term durability and less than 4 % H_2O_2 formation as compared to Pt/C. Such behavior was attributed to the strong interaction between the Cu-N_x active sites and the C_3N_4 matrix [24]. The increment in the catalyst's durability was reported when using g-C_3N_4 and Pd-aided nanocomposites and was reported to have only 8 % activity loss as compared to 45 % loss demonstrated by commercial 10 wt% Pt/C in Oxygen Reduction Reaction (ORR) [25].

Despite extensive research on bismuth-based materials, nano-composites of BiOCl with g-C_3N_4 haven't been reported yet on their electrocatalytic activity for eCO_2RR. In this work, a range of BiOCl/g-C_3N_4 composites have been synthesized, as well as morphologically, structurally and chemically characterized, and tested for their eCO_2RR activity. Uniform distribution of the oxychloride nanoplates over the g-C_3N_4 surface is desired to expose more active sites for CO_2 reduction fostering the catalytic activity.

2. Experimental

2.1. Materials used

Melamine (CAS Number 108–78-1, Sigma-Aldrich), $Bi(NO_3)_3{\cdot}5H_2O$ (CAS Number 10035–06-0, Chempur), NaCl (CAS Number 7647–14-5, Fluka), Glycine (CAS Number 56–40-6, Fluka), Nafion™ 117 (CAS Number 31175–20-9, Sigma-Aldrich) were all purchased in reagent grade and used without further purification. $KHCO_3$ (CAS Number 298–14-6, 99.999 %) was purchased from Sigma-Aldrich.

2.2. Synthesis procedure

BiOCl: 23.376 mg of NaCl was dissolved in 10 mL of bi-distilled water and was heated to 90 ℃. To it, 194.028 mg of $Bi(NO_3)_3{\cdot}5H_2O$ in 5 wt% glycine solution was added dropwise. The reaction mixture was reacted at 90 ℃ at 400 rpm for 2 h. A pearl-white precipitate was obtained which was washed three times with bi-distilled water and once with ethanol. The material was then dried in a vacuum oven at 40 ℃ for 16 h.

g-C_3N_4: It was prepared according to a procedure reported in the literature [26] using melamine decanted in a half-covered crucible and directly heating it at 550 ℃ for 3 h under static air in a muffle furnace. The obtained powders were then ball-milled for 20 min at 20 Hz, sieved, and washed with bi-distilled H_2O and ethanol.

2.2.1. BiOCl/g-C_3N_4 composite

Sol A: in a round bottom flask containing 10 mL bi-distilled water, 23.376 mg of NaCl and the required amount of g-C_3N_4 were stirred and sonicated for 2 h.

Sol B: in a beaker, 194.028 mg of $Bi(NO_3)_3{\cdot}5H_2O$ was stirred in 10 mL 5 wt% glycine solution.

Sol A was heated till 90 ℃ and then Sol B was added dropwise to it. The reaction mixture was reacted at 90 ℃ for 2 h. The precipitate was washed three times with bi-distilled water and once with ethanol, and then dried under vacuum at 40 ℃ for 16 h. Thus, the obtained composites were 12 wt% BiOCl/g-C_3N_4 (12 % BCN), 52.1 wt% BiOCl/g-C_3N_4 (52.1 % BCN), 71.2 wt% BiOCl/g-C_3N_4 (71.2 % BCN) and 80.1 wt% BiOCl/g-C_3N_4 (80.1 % BCN).

2.3. Structural and morphological characterization

The morphology of the synthesized materials was investigated by

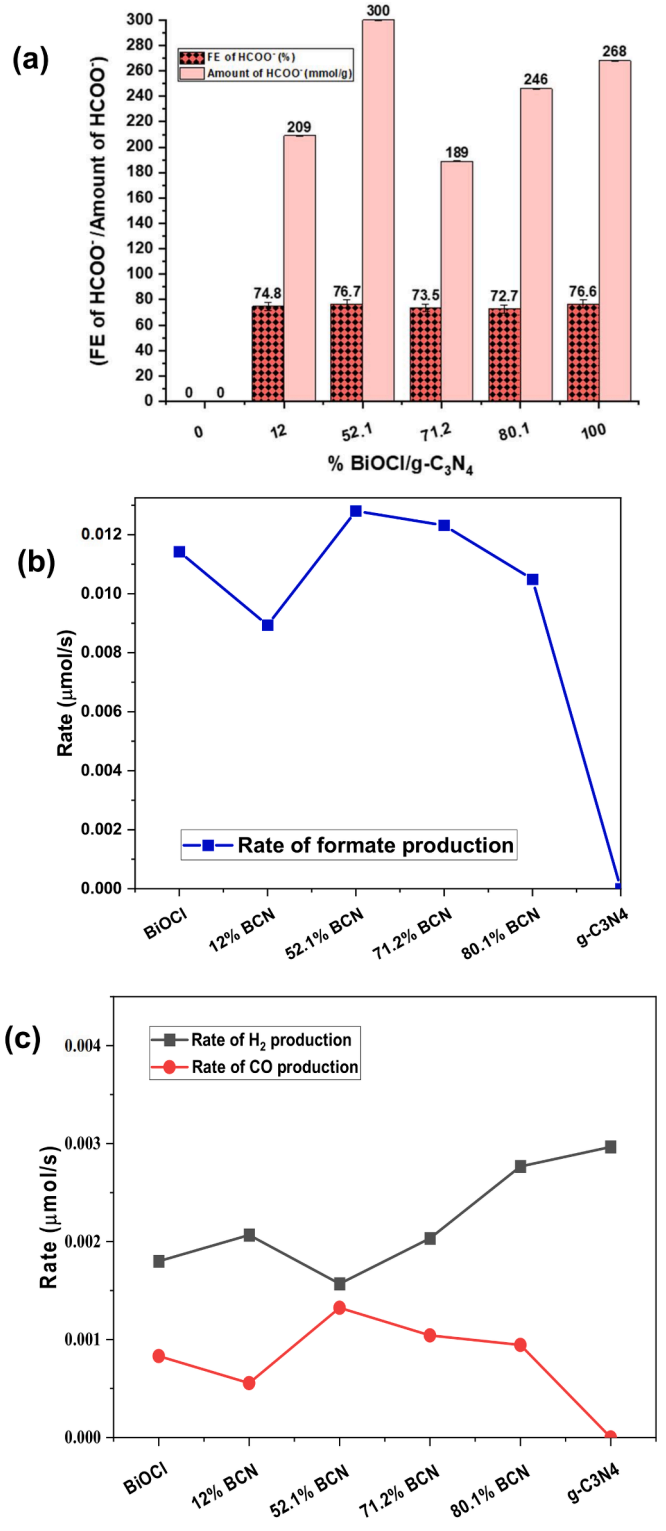

Fig. 4. Electrochemical CO_2 reduction tests at −1.06 V vs RHE for 5400 s using gas-tight cell (a) FE and amount of $HCOO^-$ for all the catalysts. (b) Rate of formate production for all the different catalysts. (c) Rate of H_2 and CO production for all the different catalysts.

Scanning Electron Microscopy (SEM) using Nova NanoSEM 450 at an accelerating voltage of 5 kV. X-ray Diffraction (XRD) study was carried out to understand the crystalline nature of the catalysts on PANalytical X'Pert Pro MPD instrument with Cu Kα radiation (λ = 0.1541 nm). Raman spectra were acquired using an Invia Reinshaw spectrometer equipped with a diode laser (λ = 785 nm). N_2 physisorption was performed with a Micrometrics ASAP 2020 analyzer at liquid nitrogen temperature. All the catalysts were degassed at 120 C for 12 h before analysis. The specific surface area was calculated by applying the BET equation. Pore size distributions were determined with the desorption branch of the isotherms with the Barrett-Joyner-Halenda (BJH) method. XPS analysis was carried out employing an in-house built apparatus consisting of an analysis chamber operated in a base pressure of about $1x10^{-9}$ mbar for these experiments, a hemispherical analyzer (VSW-HA100) equipped with a 16-channel detector which was operated in normal incidence and was served by a differential pumping system. The employed source is a non-monochromatic Al Kα (1486.7 eV, VSW-TA10). Samples were insulated to avoid differential charging using Kapton foils [27]. The analysis was carried out cooling down the system to 160 K using liquid nitrogen to minimize the thermal degradation of the samples. The Infrared (IR) spectra were recorded with an Affinity-1 S Shimadzu FT-IR, equipped with a QATR accessory, diamond crystal.

2.4. Electrochemical measurements

The electrochemical measurements were carried out in two types of cells at room temperature. For the analysis of the gaseous products, a gas-tight cell connected to an online gas chromatography unit was used. This homemade cell, designed on the model of the commercial prototype Dr. Bob™ cell, has the anodic compartment separated from the cathodic compartment via a glass tube equipped with a Vycor™ frit. A Pt wire (1.00 mm thick, 99.9 % purity, Sigma Aldrich) serves as the counter electrode inserted in the glass tube containing the electrolyte. Ag/AgCl (KCl_{SAT}) and a carbon paper electrode (Toray Carbon Paper,® 2.5 x 0.5 cm) serve as the reference and working electrode support respectively. 12 mL of the electrolyte contained in the single compartment of the cell was purged in with Ar or CO_2 at a flow rate of 20 mL min^{-1} for 25 min before starting the electrochemical measurements. This was done to saturate the electrolyte with the respective gases. The same flow rate was later maintained for the electrochemical measurements as well. Another type of three-electrode cell, equipped with a Rotating Disc Electrode (RDE, Autolab, diameter = 5 mm) was used for the preliminary electrochemical characterization. This three-electrode configuration contained a saturated calomel electrode (SCE) as the reference electrode and Pt as the counter electrode. The RDE glassy-carbon electrode with fixed area (0.19 cm^2) served as the working electrode support. 0.1 M $KHCO_3$ was used as the electrolyte for this setup as well. The electrochemical experiments were performed using a Metrohm Autolab PG302N electrochemical workstation. Moreover, the difference in performance of the catalysts in the two different cells was also investigated (Fig. S5).

The preliminary electrochemical characterization was evaluated using linear sweep voltammetry (LSV) in the potential range of 0 V to −1.1 V vs RHE using the RDE setup described in Fig. S1. Before such electrochemical measurements, cyclic voltammetry (CV) scans were carried out sweeping across a potential range of 0 V to −0.8 V vs RHE with a scan rate of 0.1 V/s. This was necessary to ensure the removal of any additional species covering the electrode surface. Then, the LSVs were recorded at a rotation speed of 1600 rpm with 5 mV/s as scan rate in Ar and CO_2 saturated electrolyte. The Ar saturated electrolyte served as a blank test to the CO_2 atmosphere.

3. Results and discussion

3.1. Characterization of catalysts

The morphological information of the prepared materials can be obtained by SEM analysis. BiOCl was formed as irregular aggregated nanoplates with an average diameter of 105 nm and a mean thickness of 17 nm (Fig. 1a) while g-C_3N_4 was present in its bulk form with aggregated sheets (Fig. 1b). SEM analysis of BiOCl/g-C_3N_4 nanocomposites

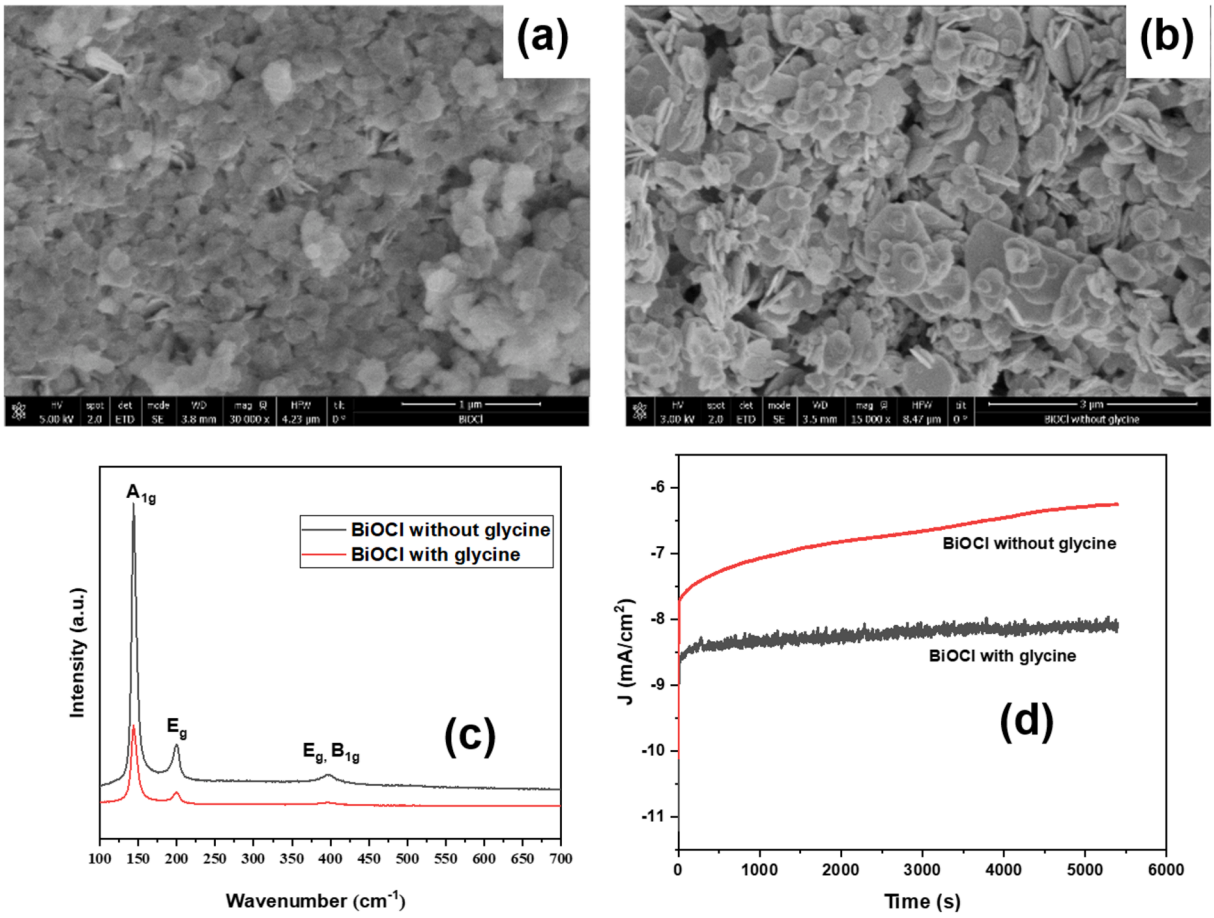

Fig. 5. (a) SEM image of BiOCl nanoplates synthesized with glycine. (b) SEM image of BiOCl microplates synthesized without glycine. (c) Raman spectra showing the correct formation of BiOCl without glycine. (d) CAs of BiOCl with and without glycine with scan interval of 1 s.

(Fig. 1c-f) showed that g-C_3N_4 particles are homogeneously covered by BiOCl nanoplates, irrespectively from the composition of the material.

The formation of the pure form of BiOCl can be confirmed by the proper indexing of XRD patterns (Fig. 2a) to the tetragonal phase of BiOCl with reflections appearing at $2\theta = 11.9^{\circ}$ (001), 24.09° (002), 25.9° (101), 32.5° (110), 33.4° (102), 34.7° (111), 36.5° (003), 40.9° (112), 46.6° (200), 48.4° (201), 49.7° (113) (JCPDS card no. 06–0249) [19]. The crystalline structure of g-C_3N_4 was also confirmed with the XRD spectrum. The reflections indexed at 12.95° and 27.34° corresponded to the (100) plane of characteristic packing of tri-s-triazine units and (002) facet of graphitic structure respectively [26]. As seen in Fig. 2a, the XRD patterns of both g-C_3N_4 and BiOCl are evident in the formation of composites. However, a progressive decline in the intensity of g-C_3N_4 reflections in the composite materials is justifiable due to the higher scattering properties of heavy atoms of BiOCl. It must be underlined that, in all the patterns related to BiOCl phase, the (*hkl*) reflections with $l = 0$ (directions orthogonal to c axis) show very sharper peaks with respect to the reflections with $l \neq 0$. This is an indication of formation of BiOCl nanoplates elongated along the a and b directions and thinned along the c direction. This result is consistent with the nanoplates' formation observed by SEM.

Raman spectroscopy was carried out for all the different materials under 785 nm excitation. Fig. 2b shows the Raman active modes of BiOCl as well as g-C_3N_4. BiOCl has its strong bands existing at 142 cm^{-1} and at 198 cm^{-1} which can be assigned to A_{1g} internal Bi-Cl stretching mode and E_g external Bi-Cl stretching mode, respectively. The weak signal at 396 cm^{-1} signifies E_g and B_{1g} vibration modes produced by the motorial oxygen atoms of the oxyhalide [28]. The intensity of the respective peaks appears to diminish in the composites with the decrease in their respective loadings. Moreover, for g-C_3N_4 the characteristic peaks can be observed in all the composites. The peak at 1232.8 cm^{-1} can be ascribed to sp^2 carbon bending vibration and the pair of peaks at 753.7 cm^{-1} and 703.4 cm^{-1} to the layer-layer deformation vibrations of g-C_3N_4 were also evident [29]. The characteristic D band and G band of g-C_3N_4 can also be found at peaks 1480.2 cm^{-1} and 1560.7 cm^{-1}, respectively [30].

N_2 sorption analysis at the liquid nitrogen temperature of pristine g-C_3N_4, BiOCl and the composite 52.1 % BCN shows type IV isotherm with H3 hysteresis loop (Fig. 2c). BET surface areas were calculated, showing a surface area of 12 $m^2\ g^{-1}$ for the composite material as compared to the pristine g-C_3N_4 and BiOCl with surface areas of 8 $m^2\ g^{-1}$ in both cases. These values confirm the synergy between BiOCl and g-C_3N_4 is crucial to improve the properties of nanocomposites with respect to the pristine counterparts. Despite low surface areas, pore size distribution (Fig. 2d) showed a broad distribution, ranging from 2 to 200 nm, suggesting the formation of mesopores as well as macropores [31]. It can be noted that the mesoporosity is higher in the composite 52.1 % BCN than in BiOCl and in g-C_3N_4. This synergistic presence of *meso* and macropores in a proper balance could positively affect the performance of the catalysts in obtaining the aimed efficiency and product yield. Thus, in the case of the composite 52.1 % BCN, the observed bimodal pore structure in the layer of the electrocatalyst could provide a disparity of pressure. This means that the bimodal structure of the pores allows the presence of pressure difference on the electrode surface. It enables the liquid reactant to diffuse into the surface of the electrocatalyst layer, which therefore enhances the electrocatalytic activity with this characteristic. Thus, the liquid reactant i.e. CO_2 saturated 0.1 M $KHCO_3$ could diffuse into the electrocatalyst layer more easily reducing the

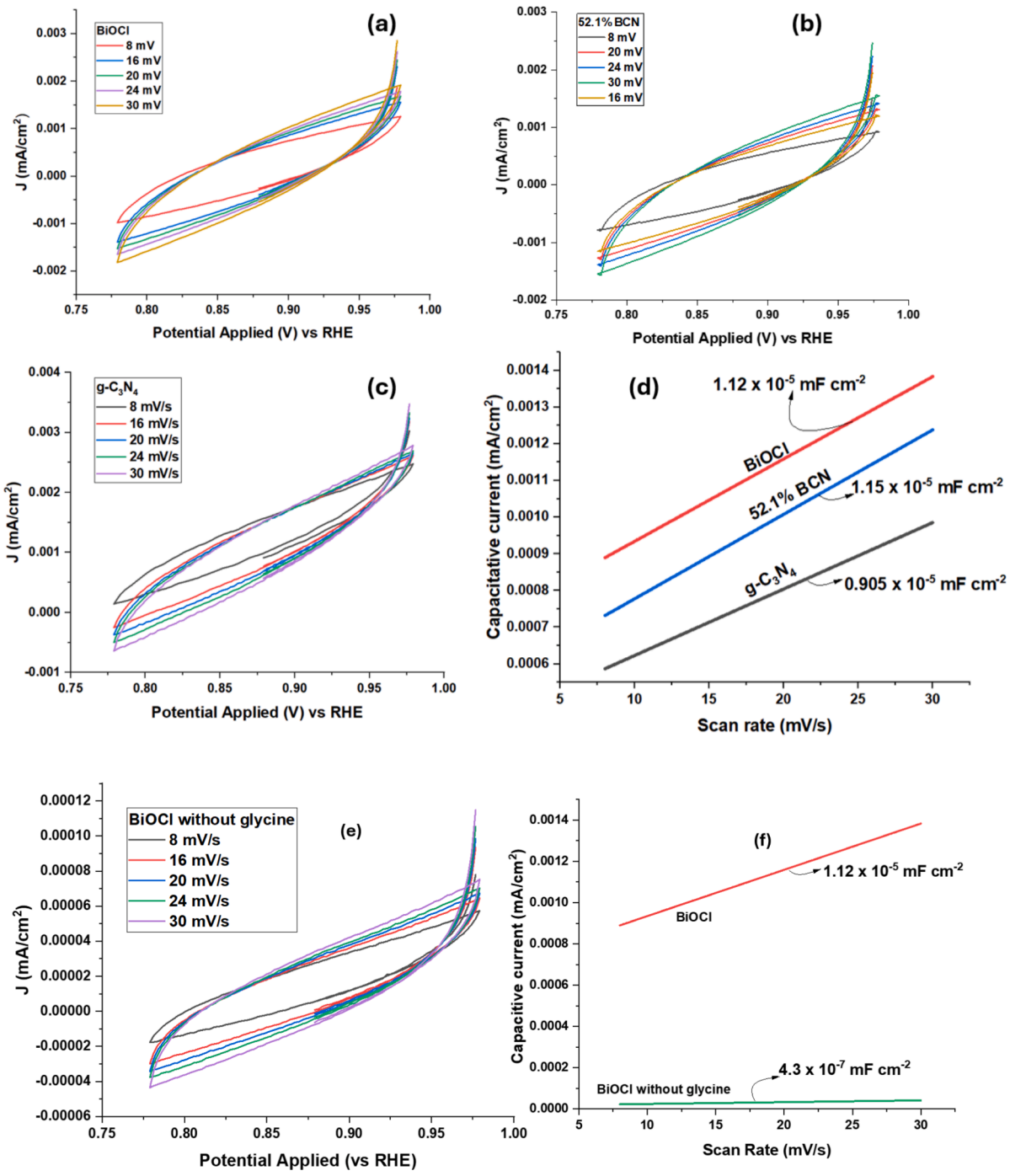

Fig. 6. CV scans across potentials 0.77 V to 0.97 V with non-faradaic process for (a) BiOCl, (b) 52.1 % BCN, (c) g-C_3N_4 (e) BiOCl without glycine (d) Capacitive current density plots at different CV scan rates; the current densities were obtained from double-layer charge/discharge curves at 0.88 V vs RHE. (f) Capacitive current density plot for BiOCl and BiOCl without glycine.

liquid sealing effect [32].

3.2. CO_2 electroreduction tests

The CO_2 electroreduction performances have been evaluated for BiOCl, g-C_3N_4, and all the other composites (12 % BCN, 52.1 % BCN, 71.2 % BCN, 80.1 % BCN). Fig. S1 provides the LSV curves for all the materials in Ar and CO_2 atmosphere conducted in the RDE set-up. We can note the increase in the current density in the CO_2-saturated 0.1 M $KHCO_3$ as compared to the inert atmosphere. This increment in the cathodic current densities can be attributed to the potential catalytic activity in eCO_2RR. The onset potential, as observed from the LSVs for BiOCl (Fig. S1), was determined to be −0.81 V vs RHE whereas for 52.1 % BCN the value equaled −0.67 V vs RHE. Considering the onset potentials, CA analyses were recorded at −0.86 V and −1.06 V vs RHE to evaluate the behavior of the catalysts in eCO_2RR. Applying −0.86 V and −1.06 V vs RHE, a CA of 5400 s was recorded in the case of BiOCl and 52.1 % BCN by the RDE set-up as a preliminary investigation (Fig. S2). $HCOO^-$ was detected as the liquid product analyzed by ion chromatography. At −0.86 V vs RHE, the FE_{HCOO}^- values of BiOCl and 52.1 % BCN were 76 % and 26 % and the amounts of $HCOO^-$ produced were 39 and 19mmol $g^{-1}h^{-1}$, respectively. At −1.06 V vs RHE, the FE values of BiOCl

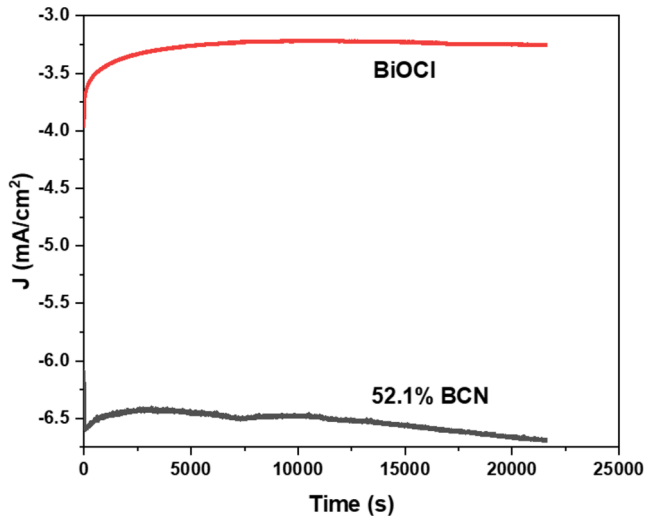

Fig. 7. Chronoamperometry curves of 52.1 % BCN composite and BiOCl for 6 h with 0.1 M $KHCO_3$ electrolyte with glassy carbon electrode with a scan interval of 5 s.

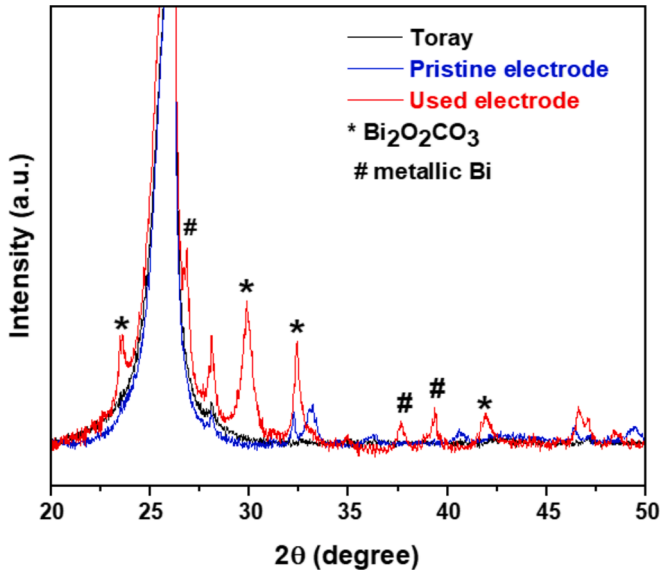

Fig. 8. XRD patterns of Toray carbon paper, BiOCl on Toray carbon paper electrodes before CA and after CA duration of 2 h. Conditions: −1.06 V vs RHE, 0.1 M $KHCO_3$ electrolyte, three-electrode gas-tight cell. The used electrode was secured with Kapton tape to avoid any air contact. In the spectra, the asterisk (*) represents the reflections corresponding to $Bi_2O_2CO_3$ and that of hash mark (#) represents the reflections corresponding to metallic Bi.

Table 1
XPS analysis with ratio determination of Bi/O and Bi/Cl [41–47].

Sample	Bi/O	Bi/Cl
BiOCl powder	1.0	1.3
52.1 % BCN powder	1.0	1.3
BiOCl before LSV	1.3	1.3
52.1 % BCN before LSV	1.3	1.1
BiOCl post LSV	1.0 (0.30 with OH/CO_3 component)	–
52.1 % BCN post LSV	1.2 (0.90 with OH/CO_3 component)	–
BiOCl post catalysis	1.5 (0.50 with OH/CO_3 component)	–
52.1 % BCN post catalysis	2.0 (0.50 with OH/CO_3 component)	–

Table 2
XPS results and binding energies (B.E.) of the fitting curves with species identification.

Sample	Bi 4f $_{7/2;5/2}$ (eV)	Cl 2p $_{3/2;1/2}$ (eV)	O 1 s (eV)
BiOCl powder	159.5;164.8 Bi^{3+} BiOCl [41–43] 159.0;164.3 Bi^{3+} Bi_2O_3 [41] 157.6;162.9 Bi^{3+} [41,48]	198.2; 199.8Cl^- [43,44]	530.4 Bi-O [43,47,49] 532.1 Bi-OH/Bi-CO_3 [43,47,49]
52.1 % BCN powder	159.4;164.7 Bi^{3+} BiOCl 158.9;164.2 Bi^{3+} Bi_2O_3	198.2; 199.8Cl^-	530.4 Bi-O 532.1 Bi-OH/Bi-CO_3
BiOCl before LSV	159.7;165.0 Bi^{3+} BiOCl	198.2; 199.8Cl^-	530.5 Bi-O 532.7 water 534.7 polymer [45,46]
52.1 % BCN before LSV	159.6; 164.9 Bi^{3+} BiOCl	198.2; 199.8Cl^-	530.5 Bi-O 532.8 water 534.7 polymer
BiOCl post LSV	159.7;165.0 Bi^{3+} compound 158.5; 163.8 Bi^{3+} Bi_2O_3	–	530.5 Bi-O 531.8 Bi-OH/Bi-CO_3 533.8 polymer
52.1 % BCN post LSV	159.5;164.8 Bi^{3+} 158.8;164.1 Bi^{3+} Bi_2O_3	198.2; 199.8Cl^-	530.5 Bi-O 531.8 Bi-OH/Bi-CO_3 534.7 polymer
BiOCl post catalysis	159.6;164.9 Bi^{3+} compound	–	530.5 Bi-O 531.9 Bi-OH/Bi-CO_3 534.0 polymer
52.1 % BCN post catalysis	160.1;165.4 Bi^{3+} compound	–	530.6 Bi-O 531.9 Bi-OH/Bi-CO_3 534.7 polymer

and 52.1 % BCN were 52 % and 82 %, and subsequently the amounts of $HCOO^-$ were 609 and 670mmol $g^{-1}h^{-1}$, respectively. From the values obtained with preliminary tests, it can be understood that 52.1 % BCN performs with the highest FE and $HCOO^-$ production value at −1.06 V vs RHE. Fig. S3 provides the CA carried out for 3600 s and FE values of 52.1 % BCN in a gas-tight cell to confirm the evolution of products as a result of eCO_2RR by using Ar atmosphere as a blank. Along with $HCOO^-$, H_2 and CO also evolved in CO_2 atmosphere while only H_2 evolved in the case of Ar. Therefore, considering −1.06 V as the optimized potential, in the following section, analysis of the products and the determination of their FE values varying with the variation in the composite composition are investigated.

To obtain a better understanding of the efficiency and selectivity properties of the prepared electrocatalysts, CA in CO_2-saturated atmosphere (Fig. 3a) at a constant potential of −1.06 V vs RHE were performed for all the different composites as well as the pristine BiOCl and g-C_3N_4 in the gas-tight cell for 5400 s. For the quantitative analyses of the products evolved, gas chromatography and ion chromatography analyses were carried out at the end of those electrochemical measurements at 5400 s. The catalysts were seen to form $HCOO^-$ as the major product and H_2 and CO as minor products. The selectivity of the products' formation was particularly high for formate accounting for 70 % to 77 % (Fig. 3b) with H_2 and CO just forming minimal amounts. For H_2, the value ranges from 9-19 % for all the catalysts except g-C_3N_4 which is equal to 96 %. Similarly, the FE values for CO range from 1-2 % for all the catalysts except g-C_3N_4 for which there is no production of CO. Among all the catalysts, noting the similar FE values for $HCOO^-$, the product yield was calculated. 52.1 % BCN produced the highest yield of $HCOO^-$ equating to 200mmol $g^{-1}h^{-1}$ as compared to all the other catalysts as shown in Fig. 4a, in addition to possessing the highest current values (Fig. 3a). Pristine BiOCl produced 179mmol $g^{-1}h^{-1}$ under the same conditions. Moreover, in the case of the composite 52.1 % BCN, the uniform distribution of the oxychloride nanoplates over g-C_3N_4 allows for increased availability for the electrolyte-catalyst interaction, directly

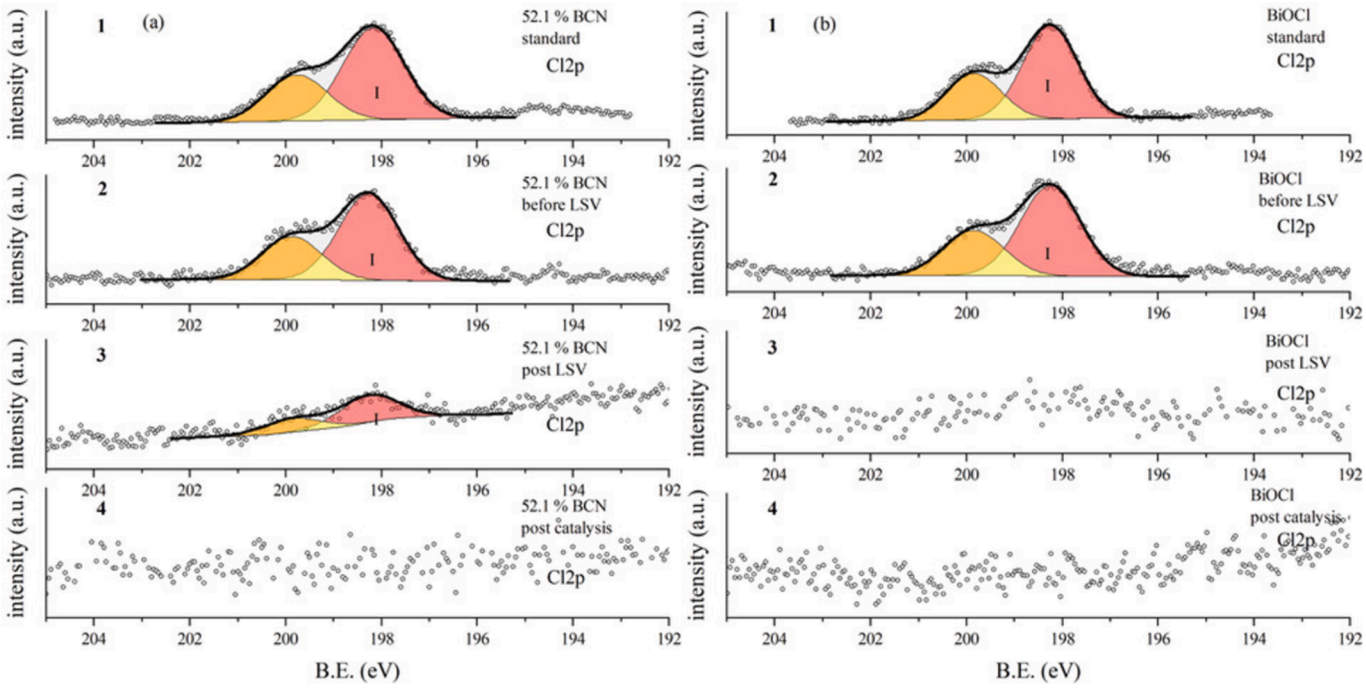

Fig. 9. XPS analysis of Cl 2p spectra of (a) 52.1% BCN and (b) BiOCl in the different stages of eCO_2RR including (1) powdered catalyst, (2) dropcast on carbon paper before LSV measurement, (3) post-LSV, and (4) post-catalysis.

affecting the production rates of the products shown in Fig. 4b and 4c. The variation in the composite percentages instigated an effective distribution allowing for sufficient exposure of the active sites of the nanoplates. This can be attributed to the availability of sufficient facets of BiOCl exposed in the catalysts. Pristine BiOCl nanoplates observed in the SEM images were seen to agglomerate which also resulted in lesser surface area as confirmed by N_2 adsorption–desorption isotherm. In addition, the composites with a higher percentage of BiOCl (71.2 %, 80.1 %) had a lower rate of reaction as well as a lower amount of produced formate. This can be attributed to the over-saturation of the nanoplates on the g-C_3N_4 surface disallowing sufficient exposure of the active facets to the CO_2-infused electrolyte.

An interesting electrocatalytic difference was noted for BiOCl which was synthesized with and without the size-controlling agent, glycine. Fig. 5a and 5b compare representative SEM images collected for BiOCl synthesized with and without glycine. It's evident that glycine is crucial to limit the growth of nanocrystal, forming microplates when glycine is not used. BET surface area of BiOCl microplates and nanoplates were very similar (8 m^2 g^{-1}). However, BiOCl microplates possess a lower pore volume as a result of a pore size distribution centered at larger diameter (Fig. S6). Moreover, as seen in Fig. 5c, BiOCl synthesized without glycine has a higher intensity in the Raman spectra if compared to BiOCl synthesized with glycine, which explains the higher crystallites formed in the case of the BiOCl microplates. IR spectroscopy was carried out for BiOCl synthesized with glycine, BiOCl synthesized without glycine, and pure glycine (Fig. S8). The signal at 3554 cm^{-1} and 1630 cm^{-1} for BiOCl synthesized without glycine and at 3559 cm^{-1} and 1618 cm^{-1} for BiOCl synthesized with glycine can be attributed to OH symmetrical stretching and scissoring, respectively. The signals located at 511 cm^{-1} and 493 cm^{-1} can be ascribed to Bi-O bonds and the signals at 1445 cm^{-1} and 1395 cm^{-1} can be attributed to stretching vibrations of BiOCl for BiOCl synthesized with and without glycine respectively. Again, in the case of pure glycine, the signal at 3150 cm^{-1} can be ascribed to NH_3^+ stretching vibrations. The signal at 1495 cm^{-1} can be attributed to symmetric stretching of COO^- group. Again, 1324, 692, 493 cm^{-1} can be attributed to CH_2 twisting, COO^- bending and COO^- rocking respectively. The signals at 1108, 1029, 891 and 606 cm^{-1} can be ascribed to NH_3^+ rocking, CCN asymmetric stretching, CCN symmetric stretching and COO^- wagging vibrations respectively [33,34]. It has been reported in literature studies that the presence of amino acids could facilitate the adsorption of CO_2 with the presence of N sites. However, in the case of BiOCl synthesized with glycine, the NH_3^+ stretching and rocking vibrations are absent which excludes the contribution of glycine in eCO_2RR [35].

To compare the current densities between both catalysts, a WE with a fixed geometrical area of 0.19 cm^2 was used. The obtained current densities with the CA analyses have been shown in Fig. 5d. A clear difference in the current densities is seen with a higher value for BiOCl synthesized with glycine if compared to the one without. The FEs were calculated for both cases as well as the amount of $HCOO^-$ was calculated. This setup wasn't gas-tight due to which the evaluation of gaseous products was not possible. BiOCl synthesized with the size-controlling agent produced nanoplates forming 957 ± 2mmol $g^{-1}h^{-1}$ of formate with 85 % of FE while BiOCl synthesized without it produced 39 ± 2mmol $g^{-1}h^{-1}$ of $HCOO^-$ with 4 % of FE after 5400 s of C.A. at −1.06 V vs RHE. This can be attributed to the nano-structuration of BiOCl and effective size tuning (Fig. 5a and 5b) which has been proven to affect the adsorption of CO_2 as studied by Liu et al. in 2021 [36]. It must be considered that productivity values in mmol $g^{-1}h^{-1}$ are reported for comparison with the reported literature since current values are not constant in all the chronoamperometries throughout the work.

The Electrochemical Surface Area (ECSA) for the pristine material i.e. BiOCl, BiOCl synthesized without glycine, g-C_3N_4 and 52.1 % BCN were evaluated using the glassy carbon electrode with fixed geometrical area (0.19 cm^2). The CV measurements were recorded in 0.1 M $KHCO_3$ electrolyte which was Ar saturated with the electrode at 1200 rpm as shown in Fig. 6. The scan rates to carry out the CV response of the prepared electrodes were 8 mV/s, 16 mV/s, 20 mV/s, 24 mV/s, and 30 mV/s across a potential range from 0.77 V to 0.97 V vs RHE. This potential range was chosen to avoid the contribution of any faradaic processes. Further, the ECSA was calculated as follows:

$$ECSA = R_f{}^*S \quad (3)$$

where R_f denotes the roughness factor. It is defined as the ratio of the

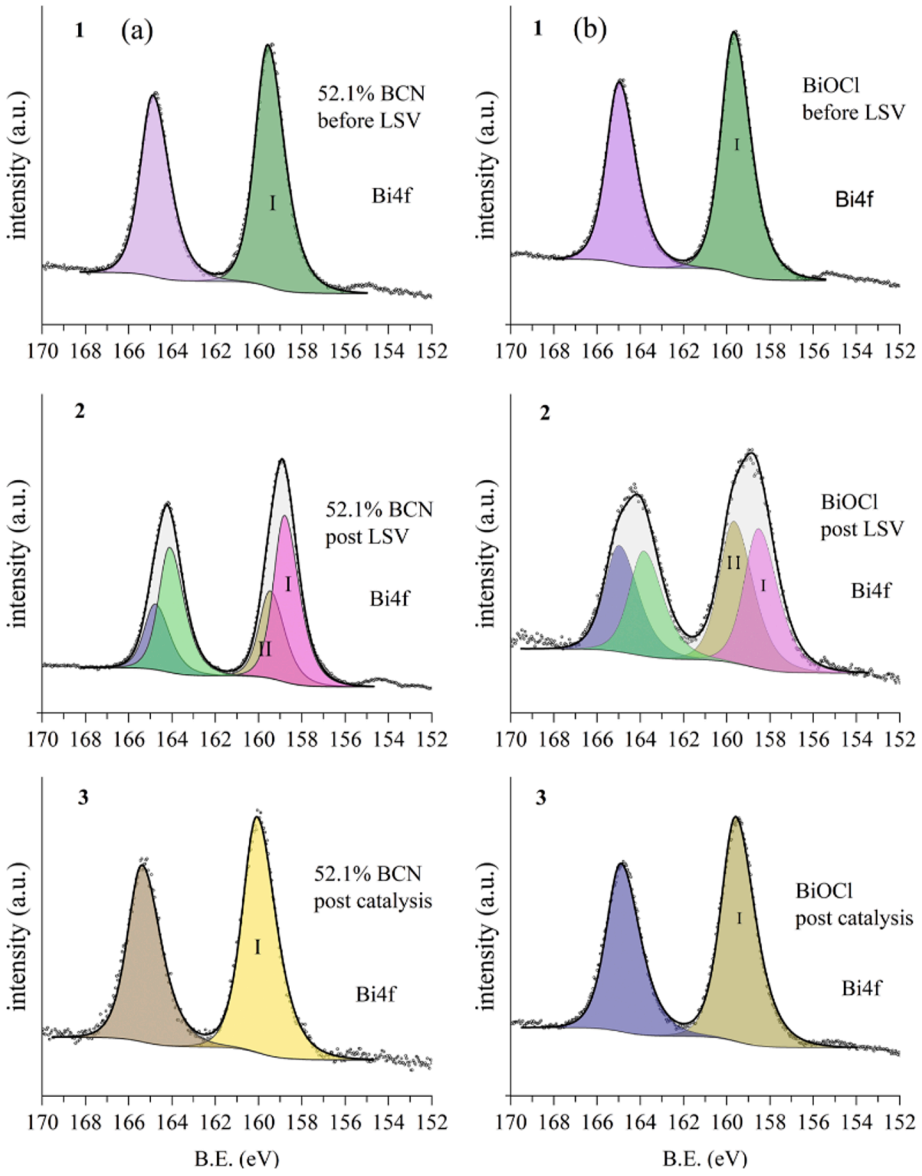

Fig. 10. XPS analysis of Bi 4f spectra of (a) 52.1% BCN and (b) BiOCl in the different stages of eCO_2RR including (1) catalyst dropcast on carbon paper before LSV measurement, (2) post-LSV, and (3) post-catalysis.

double layer capacitance C_{dl} of the working electrode to that of the corresponding smooth glassy carbon electrode. S represents the geometrical surface area of the smooth glassy carbon electrode support. The C_{dl} value can be determined by establishing a linear relationship between $\Delta j = (j_a - j_c)$, where j_a and j_c denotes the anodic and cathodic current density, respectively, considering the values at the scan rate at 0.88 V vs. RHE. The C_{dl} value of the smooth glassy carbon was determined to be 0.65 x 10^{-5} mF cm^{-2}. Fig. 5a, 5b, 5c and 5e show the various CV scans carried out at the scan rates mentioned above for BiOCl, BiOCl synthesized without glycine, 52.1 % BCN, and g-C_3N_4 respectively. We determined the R_f values to be 1.73, 0.06, 1.39, and 1.77 while ECSA values to be 0.33 cm^2, 0.01 cm^2, 0.26 cm^2, and 0.34 cm^2 for BiOCl, BiOCl synthesized without glycine, g-C_3N_4, and 52.1 % BCN, respectively. Moreover, CO_2 adsorption studies were carried out at 304 K and BiOCl was seen to have a higher adsorption isotherm followed by 52.1 % BCN and then g-C_3N_4 (Fig. S7). It must be taken into account that these studies involve CO_2 adsorption, where CO_2 in its gas phase is adsorbed on the solid surface of the catalyst. However, it has been reported that eCO_2RR involves the interaction of carbonic acid with the solid catalysts [37,38].

Additional electrochemical CO_2 reduction processes such as extended duration CA were recorded and the catalyst on the formation of the composite was also tested. The CA curves are shown in Fig. 7. The glassy carbon-based electrode support was used for these studies where the same electrode was used for 6 h of continuous bias application. CAs were run at −1.06 V vs RHE in CO_2-saturated 0.1 M $KHCO_3$ with the pristine BiOCl and the composite 52.1 % BCN. FE values of BiOCl and 52.1 % BCN equaled 77 % and 73 % with $HCOO^-$ amounts equivalent to 357 ± 1 mmol $g^{-1}h^{-1}$ and 678 ± 1 mmol $g^{-1}h^{-1}$ with CA for 6 h, respectively.

3.3. Post-characterization of the catalysts

To gain insight into the structural and morphological information of the catalyst, post-eCO_2RR characterization was carried out. Characterization techniques such as XRD and XPS were employed for the pristine BiOCl and the composite 52.1 % BCN.

XRD patterns have been collected on the BiOCl carbon paper electrodes pre-catalysis and post-catalysis and were compared with the pristine BiOCl material (Fig. 8). It must be underlined that the post-

catalysis electrode was immediately sealed within two Kapton adhesive tapes to avoid long exposure to air. The XRD pattern of the post-catalysis electrode indicates the presence of $Bi_2O_2CO_3$ as well as metallic Bi. The reflections at 12.59°, 23.64°, 25.74°, 30.03°, 32.50°, 39.10°, 42.05°, 46.75°, 51.97°, and 54.27° can be indexed to (002), (011), (004), (013), (110), (006), (114), (020), (121), and (123) of $Bi_2O_2CO_3$ [39]. Similarly, the reflections at 27.12°, 38.03°, and 39.67° can be attributed to (012), (104), and (110) crystallographic planes of metallic Bi (JCPDS 05–0519) [40]. Additional peaks appearing in the spectra are attributed to the non-subtracted peaks of carbon Toray paper. It must be also acknowledged that the ex-situ XRD technique limits the information on the phase evolution of the catalyst.

XPS characterization was also performed on BiOCl and 52.1 % BCN before and after eCO_2RR. The XPS analysis was carried out in the powders of the catalyst, the catalyst dropcasted on the electrodes, the electrodes after running an LSV, and the electrodes post-catalysis. It is evident from the elemental composition as well as the data analysis of the regions of interest that the ink deposition step in the electrodes did not induce any degradation of the BiOCl (Table 1 and Table 2). Post-LSV, both materials showed a marked loss of chloride (Table 1, Fig. 9a and 9b) and a formation of two different species of bismuth (Table 2, Fig. 10a and 10b), one ascribable to Bi^{3+} as Bi_2O_3 and the other to Bi^{3+} in presence of either oxygen vacancies or a formation of a different Bi^{3+} compound such as $Bi_2O_2CO_3$, following the high amount of oxygen attributable to carbonated species. The content of chlorine, in the post-catalysis series, results in the accessible area (thus within the first 5–10 nm from the surface) below the detection limit of the technique in both of the samples, bismuth has been identified as Bi^{3+} (single component) ascribable to a compound with a bismuth to oxygen ratio higher than the one of Bi_2O_3, more resembling the one of $Bi_2O_2CO_3$ (Table 1). XPS analysis of O 1 s spectra of all the stages of BiOCl and 52.1 % BCN are presented in Fig. S4.

4. Conclusions

In a conclusive view, BiOCl when synthesized into nanoplates has higher catalytic activity as compared to microplates. It was seen how the use of the size-controlling agent glycine aided in the nanostructuration of the catalyst. Further, effective uniform deposition of BiOCl nanoplates on g-C_3N_4 allowed for sufficient exposure of the active sites of the catalyst which in the case of 52.1 % BCN allowed for uniform deposition and hence allowed for its highest catalytic performance. Minimal production of side products like H_2 and CO gives an added advantage of increased selectivity of $HCOO^-$. 52.1 % BCN produced 200mmol $g^{-1}h^{-1}$ as compared to 179mmol $g^{-1}h^{-1}$ for pristine BiOCl at 5400 s applying −1.06 V vs RHE in a gas-tight cell. Extended hours of testing were carried out to understand the behavior of the catalyst with a longer duration. The behavior was noted to be stable for both 52.1 % BCN and BiOCl for 6 h with the yield of $HCOO^-$ being 678mmol $g^{-1}h^{-1}$ and 1428mmol $g^{-1}h^{-1}$ for 52.1 % BCN and BiOCl, respectively. The catalysts were characterized by SEM, XRD, Raman spectroscopy, IR spectroscopy, sorption analysis, and XPS, and then for post-catalysis and in the different stages of the eCO_2RR by XRD and XPS. Post-catalytic characterization has shown the presence of $Bi_2O_2CO_3$ instead of pure metallic bismuth. The bimodal pores' distribution of 52.1 % BCN further explains the improved diffusion of the electrolyte into the catalyst surface. Low production of H_2 and CO was obtained which makes this catalyst highly suitable for scale-up use considering also the simple cost-effective synthesis method.

Declaration of competing interest

The authors declare the following financial interests/personal relationships which may be considered as potential competing interests: Tiziano Montini reports financial support and article publishing charges were provided by University of Trieste. If there are other authors, they declare that they have no known competing financial interests or personal relationships that could have appeared to influence the work reported in this paper.

Data availability

Data will be made available on request.

Acknowledgements

Prof. Maurizio Prato and the staff of Materials, Energy and Environment research group at the Department of Chemical and Pharmaceutical Sciences of the University of Trieste are kindly acknowledged for the helpful discussions. We acknowledge financial support under the National Recovery and Resilience Plan (NRRP), Mission 4, Component 2, Investment 1.1, Call for tender No. 104 published on 2.2.2022 by the Italian Ministry of University and Research (MUR), funded by the European Union – NextGenerationEU – Project Title "Bio-inspired Photo-ElectroCatalytic NanoArchitectures for Energy Conversion and Storage – NANOARC" – CUP J53D23008590006 – Grant Assignment Decree No. 1064 adopted on 18.07.2023 by the Italian Ministry of Ministry of University and Research (MUR) and under the National Recovery and Resilience Plan (NRRP), Mission 4, Component 2, Investment 1.1, Call for tender No. 1409 published on 14.9.2022 by the Italian Ministry of University and Research (MUR), funded by the European Union – NextGenerationEU – Project Title Refractory plasmonic metasurfaces for solar thermal catalytic CO_2 conversion (RESOLCAT) – CUP D53D23017090001 – Grant Assignment Decree No. 1384 adopted on 01.09.2023 by the Italian Ministry of Ministry of University and Research (MUR).

Appendix A. Supplementary data

Supplementary data to this article can be found online at https://doi.org/10.1016/j.ica.2024.122395.

References

[1] S. Zhang, Z. Mo, J. Wang, H. Liu, P. Liu, D. Hu, T. Tan, C. Wang, Ultra-stable oxygen species in Ag nanoparticles anchored on g-C3N4 for enhanced electrochemical reduction of CO2, Electrochim. Acta 390 (2021) 138831, https://doi.org/10.1016/j.electacta.2021.138831.
[2] X. Ye, Y. Jiang, X. Chen, B. Guo, S. Mao, Y. Guo, C. Zhao, Insights into the template effect on nanostructured CuO catalysts for electrochemical CO2 reduction to CO, Front. Energy Res. 10 (2022) 1–14, https://doi.org/10.3389/fenrg.2022.964011.
[3] S. Bashir, S.S. Hossain, S.U. Rahman, S. Ahmed, A. Al-Ahmed, M.M. Hossain, Electrocatalytic reduction of carbon dioxide on SnO2/MWCNT in aqueous electrolyte solution, J. CO2 Util. 16 (2016) 346–353, https://doi.org/10.1016/j.jcou.2016.09.002.
[4] D. Bairrão, J. Soares, J. Almeida, J.F. Franco, Z. Vale, Green hydrogen and energy transition: current state and prospects in portugal, Energies 16 (2023) 1–23, https://doi.org/10.3390/en16010551.
[5] N. Iqbal, A. Afzal, I. Khan, M.S. Khan, A. Qurashi, Molybdenum impregnated g-C 3 N 4 nanotubes as potentially active photocatalyst for renewable energy applications, Sci. Reports | 11 (123AD) 16886. https://doi.org/10.1038/s41598-021-96490-6.
[6] M.I. Khan, S.G. Al-Ghamdi, Hydrogen economy for sustainable development in GCC countries: a SWOT analysis considering current situation, challenges, and prospects, Int. J. Hydrogen Energy 48 (2023) 10315–10344, https://doi.org/10.1016/j.ijhydene.2022.12.033.
[7] J. Eppinger, K.W. Huang, Formic acid as a hydrogen energy carrier, ACS Energy Lett. 2 (2017) 188–195, https://doi.org/10.1021/acsenergylett.6b00574.
[8] C. Kim, Y. Lee, K. Kim, U. Lee, Implementation of formic acid as a liquid organic hydrogen carrier (LOHC): techno-economic analysis and life cycle assessment of formic acid produced via CO2 utilization, Catalysts 12 (2022), https://doi.org/10.3390/catal12101113.
[9] Z. Yang, F.E. Oropeza, K.H.L. Zhang, P-block metal-based (Sn, In, Bi, Pb) electrocatalysts for selective reduction of CO2to formate, APL Mater. 8 (2020), https://doi.org/10.1063/5.0004194.
[10] G. Piao, G. Yu, S. Kim, J.S. Cha, D.S. Han, H. Park, Electrocatalytic carbon dioxide conversion to formate using gas-diffusion electrodes with group 12–15 metals, J. Environ. Chem. Eng. 12 (2024) 112623, https://doi.org/10.1016/j.jece.2024.112623.

[11] Q. Li, Y. Zhang, X. Zhang, H. Wang, Q. Li, J. Sheng, J. Yi, Y. Liu, J. Zhang, Novel Bi, BiSn, Bi2Sn, Bi3Sn, and Bi4Sn catalysts for efficient electroreduction of CO2 to formic acid, Ind. Eng. Chem. Res. 59 (2020) 6806–6814, https://doi.org/10.1021/acs.iecr.9b03017.
[12] E. Bertin, S. Garbarino, C. Roy, S. Kazemi, D. Guay, Selective electroreduction of CO2 to formate on Bi and oxide-derived Bi films, J. CO2 Util. 19 (2017) 276–283, https://doi.org/10.1016/j.jcou.2017.04.006.
[13] R.P. Dighole, A.V. Munde, B.B. Mulik, B.R. Sathe, Bi2O3 nanoparticles decorated carbon nanotube: an effective nanoelectrode for enhanced electrocatalytic 4-nitrophenol reduction, Front. Chem. 8 (2020) 1–10, https://doi.org/10.3389/fchem.2020.00325.
[14] T. Gao, X. Wen, T. Xie, N. Han, K. Sun, L. Han, H. Wang, Y. Zhang, Y. Kuang, X. Sun, Morphology effects of bismuth catalysts on electroreduction of carbon dioxide into formate, Electrochim. Acta 305 (2019) 388–393, https://doi.org/10.1016/j.electacta.2019.03.066.
[15] M. Melchionna, M. Moro, S. Adorinni, L. Nasi, S. Colussi, L. Poggini, S. Marchesan, G. Valenti, F. Paolucci, M. Prato, P. Fornasiero, Driving up the electrocatalytic performance for carbon dioxide conversion through interface tuning in graphene oxide-bismuth oxide nanocomposites, ACS Appl. Energy Mater. 5 (2022) 13356–13366, https://doi.org/10.1021/acsaem.2c02013.
[16] S. Talukdar, T. Montini, Role of Facets and Morphologies of Di ff erent Bismuth-Based Materials for CO 2 Reduction to Fuels, (2024).
[17] P.A. Hsieh, P.J. Chen, L.M. Lyu, S.Y. Chen, M.C. Tseng, M.Y. Chung, W.H. Chiang, J.L. Chen, C.H. Kuo, enhanced production of formic acid in electrochemical CO2Reduction over Pd-Doped BiOCl Nanosheets, ACS Appl. Mater. Interfaces 13 (2021) 58799–58808, https://doi.org/10.1021/acsami.1c20009.
[18] H.Q. Fu, J. Liu, N.M. Bedford, Y. Wang, J. Wright, P.F. Liu, C.F. Wen, L. Wang, H. Yin, D. Qi, P. Liu, H.G. Yang, H. Zhao, Operando converting BiOCl into Bi2O2(CO3)xCly for efficient electrocatalytic reduction of carbon dioxide to formate, Nano-Micro Lett. 14 (2022) 1–16, https://doi.org/10.1007/s40820-022-00862-0.
[19] ChemElectroChem - 2020 - Subramanian - Bismuth Oxychloride Dispersed on Nitrogen-Doped Carbon as Catalyst for the.pdf, (n.d.).
[20] L. Tong, L. Zhang, S. Melhi, D.A. Alshammari, M. Kallel, Z. Zheng, J. Yang, C. Wang, Electrochemical reduction of CO2 by graphitized carbon nitride composite anion exchange membranes: potential for high CO selectivity, Adv. Compos. Hybrid Mater. 7 (2024), https://doi.org/10.1007/s42114-024-00891-w.
[21] X. Mao, R. Guo, Q. Chen, H. Zhu, H. Li, Z. Yan, Z. Guo, T. Wu, Recent advances in graphitic carbon nitride based electro-catalysts for CO2 reduction reactions, Molecules 28 (2023), https://doi.org/10.3390/molecules28083292.
[22] Q. Gong, J. Xiong, T. Zhou, W. Bao, X. Zhang, G. Liu, G. Qiao, Z. Xu, Composite interfaces of g-C3N4 fragments loaded on a Cu substrate for CO2 reduction, Phys. Chem. Chem. Phys. (2024) 10202–10213, https://doi.org/10.1039/d3cp05818b.
[23] R. Nazir, A. Kumar, M. Ali Saleh Saad, S. Ali, Development of CuAg/Cu2O nanoparticles on carbon nitride surface for methanol oxidation and selective conversion of carbon dioxide into formate, J. Colloid Interface Sci. 578 (2020) 726–737, https://doi.org/10.1016/j.jcis.2020.06.033.
[24] S. Sarkar, S.S. Sumukh, K. Roy, N. Kamboj, T. Purkait, M. Das, R.S. Dey, Facile one step synthesis of Cu-g-C3N4 electrocatalyst realized oxygen reduction reaction with excellent methanol crossover impact and durability, J. Colloid Interface Sci. 558 (2019) 182–189, https://doi.org/10.1016/j.jcis.2019.09.107.
[25] S.K. Konda, M. Amiri, A. Chen, Photoassisted deposition of palladium nanoparticles on carbon nitride for efficient oxygen reduction, J. Phys. Chem. C 120 (2016) 14467–14473, https://doi.org/10.1021/acs.jpcc.6b02080.
[26] P. Chang, I. Tseng, Photocatalytic conversion of gas phase carbon dioxide by graphitic carbon nitride decorated with cuprous oxide with various morphologies, J. CO2 Util. 26 (2018) 511–521, https://doi.org/10.1016/j.jcou.2018.06.009.
[27] A. International, Standard Guide to Charge Control and Charge Referencing Techniques in X-Ray Photoelectron Spectroscopy, (2015). https://www.astm.org/e1523-15.html.
[28] D. Ma, J. Zhong, J. Li, C. Burda, R. Duan, Preparation and photocatalytic performance of MWCNTs/BiOCl: Evidence for the superoxide radical participation in the degradation mechanism of phenol, Appl. Surf. Sci. 480 (2019) 395–403, https://doi.org/10.1016/j.apsusc.2019.02.195.
[29] J. Jiang, L. Ou-Yang, L. Zhu, A. Zheng, J. Zou, X. Yi, H. Tang, Dependence of electronic structure of g-C3N4 on the layer number of its nanosheets: a study by Raman spectroscopy coupled with first-principles calculations, Carbon n. y. 80 (2014) 213–221, https://doi.org/10.1016/j.carbon.2014.08.059.
[30] W.J. Ong, L.L. Tan, S.P. Chai, S.T. Yong, Heterojunction engineering of graphitic carbon nitride (g-C3N4) via Pt loading with improved daylight-induced photocatalytic reduction of carbon dioxide to methane, Dalt. Trans. 44 (2014) 1249–1257, https://doi.org/10.1039/c4dt02940b.
[31] Z. Mo, H. Xu, X. She, Y. Song, P. Yan, J. Yi, X. Zhu, Y. Lei, S. Yuan, H. Li, Constructing Pd/2D-C 3 N 4 composites for efficient photocatalytic H 2 evolution through nonplasmon-induced bound electrons, Appl. Surf. Sci. 467–468 (2019) 151–157, https://doi.org/10.1016/j.apsusc.2018.10.115.
[32] S.X. Chen, X. Zhang, P.K. Shen, Macroporous conducting matrix: fabrication and application as electrocatalyst support, Electrochem. Commun. 8 (2006) 713–719, https://doi.org/10.1016/j.elecom.2006.02.016.
[33] A.C. Mera, C.A. Rodríguez, L. Pizarro-Castillo, M.F. Meléndrez, H. Valdés, Effect of temperature and reaction time during solvothermal synthesis of BiOCl on microspheres formation: implications in the photocatalytic oxidation of gallic acid under simulated solar radiation, J. Sol-Gel Sci. Technol. 95 (2020) 146–156, https://doi.org/10.1007/s10971-020-05312-0.
[34] R. Ashok Kumar, R. Ezhil Vizhi, N. Sivakumar, N. Vijayan, D. Rajan Babu, Crystal growth, optical and thermal studies of nonlinear optical γ-glycine single crystal grown from lithium nitrate, Optik (stuttg) 123 (2012) 409–413, https://doi.org/10.1016/j.ijleo.2011.04.019.
[35] M. Li, E.P. Delmo, G. Hou, X. Cui, M. Zhao, Z. Tian, Y. Zhang, M. Shao, Enhancing local CO_2 adsorption by L-histidine incorporation for selective formate production Over the wide potential window, Angew. Chem. Int. Ed. 62 (2023) e202313522.
[36] P. Liu, H. Liu, S. Zhang, J. Wang, C. Wang, Effects of thicknesses and sizes of BiOX nanoplates precursors on derived Bi nanosheets for efficient CO_2 electroreduction, J. CO2 Util. 51 (2021) 101643, https://doi.org/10.1016/j.jcou.2021.101643.
[37] R. Khakpour, D. Lindberg, K. Laasonen, M. Busch, CO2 or carbonates – what is the active species in electrochemical CO2 reduction over Fe-Porphyrin? ChemCatChem 15 (2023) https://doi.org/10.1002/cctc.202201671.
[38] H. Zhong, K. Fujii, Y. Nakano, F. Jin, Effect of CO2 bubbling into aqueous solutions used for electrochemical reduction of CO2 for energy conversion and storage, J. Phys. Chem. C 119 (2015) 55–61, https://doi.org/10.1021/jp509043h.
[39] N. Duc Van, N.M. Ha, N. Van Dung, H.T.H. Ngoc, P., Van Truong, Biosynthesis of plasmonic Ag/Bi2O2CO3 nanocomposites from Acacia hybrid leaf extract with enhanced photocatalytic activity, Inorg. Chem. Commun. 150 (2023) 110443, https://doi.org/10.1016/j.inoche.2023.110443.
[40] C. Gomez, G. Hallot, A. Pastor, S. Laurent, E. Brun, C. Sicard-Roselli, M. Port, Metallic bismuth nanoparticles: Towards a robust, productive and ultrasound assisted synthesis from batch to flow-continuous chemistry, Ultrason. Sonochem. 56 (2019) 167–173, https://doi.org/10.1016/j.ultsonch.2019.04.012.
[41] J. Chastain, R.C. King Jr, Handbook of X-ray photoelectron spectroscopy, Perkin-Elmer Corp. 40 (1992) 221.
[42] R. Phenomena, C. Engmeenng, Spectroscopic Analysis m Figs 1–5 (1982) 25.
[43] L. Armelao, G. Bottaro, C. MacCato, E. Tondello, Bismuth oxychloride nanoflakes: Interplay between composition-structure and optical properties, Dalt. Trans. 41 (2012) 5480–5485, https://doi.org/10.1039/c2dt12098d.
[44] J. Zhu, J. Fan, T. Cheng, M. Cao, Z. Sun, R. Zhou, L. Huang, D. Wang, Y. Li, Y. Wu, Bilayer nanosheets of unusual stoichiometric bismuth oxychloride for potassium ion storage and CO2 reduction, Nano Energy 75 (2020) 104939, https://doi.org/10.1016/j.nanoen.2020.104939.
[45] C. Chen, G. Levitin, D.W. Hess, T.F. Fuller, XPS investigation of Nafion® membrane degradation, J. Power Sources 169 (2007) 288–295, https://doi.org/10.1016/j.jpowsour.2007.03.037.
[46] D.W. Zeng, K.C. Yung, C.S. Xie, XPS investigation of the chemical characteristics of Kapton films ablated by a pulsed TEA CO2 laser, Surf. Coatings Technol. 153 (2002) 210–216, https://doi.org/10.1016/S0257-8972(01)01696-6.
[47] D. Ma, J. Zhong, R. Peng, J. Li, R. Duan, Effective photoinduced charge separation and photocatalytic activity of hierarchical microsphere-like C 60 /BiOCl, Appl. Surf. Sci. 465 (2019) 249–258, https://doi.org/10.1016/j.apsusc.2018.09.192.
[48] M. Ionic, of M~l, 12 (1973) 1972–1974.
[49] H. Lu, L. Xu, B. Wei, M. Zhang, H. Gao, W. Sun, Enhanced photosensitization process induced by the p-n junction of Bi 2 O 2 CO 3 /BiOCl heterojunctions on the degradation of rhodamine B, Appl. Surf. Sci. 303 (2014) 360–366, https://doi.org/10.1016/j.apsusc.2014.03.006.